Geophysical Journal International

Geophys. J. Int. (2013) doi: 10.1093/gji/ggt090

Geophysical Journal International Advance Access published April 4, 2013

Modelling secondary microseismic noise by normal mode summation

L. Gualtieri,[1,2] E. Stutzmann,[1] Y. Capdeville,[3] F. Ardhuin,[4] M. Schimmel,[5] A. Mangeney[6] and A. Morelli[7]

[1] *Institut de Physique du Globe de Paris (IPGP), UMR* 7154 *CNRS,* F-75005, *Paris, France. E-mail: gualtieri@ipgp.fr*
[2] *Dipartimento di Fisica e Astronomia, Settore di Geofisica, Università di Bologna, Bologna, Italy*
[3] *CNRS, Laboratoire de Planètologie et Gèodynamique de Nantes, Nantes, France*
[4] *Laboratoire d'Océanographie Spatiale, Ifremer, Plouzanè, Brest, France*
[5] *Institute of Earth Sciences Jaume Almera, CSIC, Barcelona, Spain*
[6] *Institut de Physique du Globe de Paris, Sorbonne Paris Cité, Univ Paris Diderot, UMR* 7154 *CNRS,* F-75005, *Paris, France*
[7] *Istituto Nazionale di Geofisica e Vulcanologia (INGV), Bologna, Italy*

Accepted 2013 March 4. Received 2013 March 1; in original form 2012 December 21

SUMMARY

Secondary microseisms recorded by seismic stations are generated in the ocean by the interaction of ocean gravity waves. We present here the theory for modelling secondary microseismic noise by normal mode summation. We show that the noise sources can be modelled by vertical forces and how to derive them from a realistic ocean wave model. We then show how to compute bathymetry excitation effect in a realistic earth model by using normal modes and a comparison with *Longuet–Higgins* approach. The strongest excitation areas in the oceans depends on the bathymetry and period and are different for each seismic mode. Seismic noise is then modelled by normal mode summation considering varying bathymetry. We derive an attenuation model that enables to fit well the vertical component spectra whatever the station location. We show that the fundamental mode of Rayleigh waves is the dominant signal in seismic noise. There is a discrepancy between real and synthetic spectra on the horizontal components that enables to estimate the amount of Love waves for which a different source mechanism is needed. Finally, we investigate noise generated in all the oceans around Africa and show that most of noise recorded in Algeria (TAM station) is generated in the Northern Atlantic and that there is a seasonal variability of the contribution of each ocean and sea.

Key words: Surface waves and free oscillations; Seismic attenuation; Theoretical seismology; Wave propagation.

1 INTRODUCTION

Microseisms are the continuous oscillation of the ground recorded everywhere in the world independently from earthquake activity in the period band between 4 and 20 s (e.g. Webb 1998; Stutzmann *et al.* 2000; Berger *et al.* 2004). This seismic background noise results from the non-linear interaction between the atmosphere, the ocean and the solid Earth. The source is the atmospheric wind which forces the ocean gravity waves generation (Miche 1944; Longuet-Higgins 1950; Hasselmann 1963). Seismic noise spectra display two main peaks at 14 and 7 s, which denote what are called respectively primary and secondary microseisms. The primary microseismic peak is the smaller amplitude hump with periods between 10 and 20 s. It is generated near the coast when ocean waves reach shallow water and interact with shallow seafloor (Hasselmann 1963). Both Rayleigh and Love waves are present in significant quantities (Nishida *et al.* 2008; Fukao *et al.* 2010). The secondary microseismic peak is the strongest noise peak with periods between 4 and 10 s. It is generated by the interaction of ocean gravity waves having similar periods and travelling in opposite directions. When two ocean waves meet each other, at first-order approximation, the resulting displacement decays exponentially with depth. Longuet-Higgins (1950) showed that the microseisms are generated by pressure fluctuations which can be computed considering the second-order term of the ocean wave interaction. Secondary microseisms are dominantly Rayleigh waves. Longuet–Higgins computed the excitation of Rayleigh waves at the ocean bottom as a function of frequency, bathymetry and *S*-wave velocity in the crust. Hasselmann (1963) extended the theory to a random ocean wavefield and showed that the matching between ocean waves and seismic waves takes place only when the interaction occurs between two ocean waves with nearly opposite directions and nearly similar frequencies.

The sea state that generates seismic noise can be classified in three classes (Longuet-Higgins 1950; Ardhuin *et al.* 2011, 2012). The first class occurs when a storm has a wide angular distribution, with ocean waves coming from many different azimuths. The first class dominates at frequencies from 0.5 to 2 Hz due to the wide angular distribution of the short waves generated by a constant and steady wind, and it may still be significant at somewhat lower frequencies. In that case, the interacting waves are within the storm.

In the second class, ocean waves arrive at the coast, they are reflected and they meet up with incident ocean waves. Then, the interaction area is confined close to the coast. The third class concerns the interaction of ocean waves coming from different storms. Ocean waves from a given storm may travel long distances before meeting ocean waves generated by another storm. This third class generates the strongest noise sources and these can be anywhere in the ocean basin. Obrebski *et al.* (2012) identified such a source located midway between Hawaii and California, and recorded by stations several thousands of kilometres away.

Secondary microseismic sources have been observed near the coast (Bromirski & Duennebier 2002; Schulte-Pelkum *et al.* 2004; Gerstoft & Tanimoto 2007; Yang & Ritzwoller 2008), in the middle of the ocean (Cessaro 1994; Stelhy *et al.* 2006; Obrebski *et al.* 2012) and in both cases (Haubrich & Mc Camy 1969; Friedrich *et al.* 1998; Chevrot *et al.* 2007). Kedar *et al.* (2008) showed the first quantitative modelling of seismic noise using ocean wave model hindcasts. They successfully modelled seismic noise generated in deep ocean—North Atlantic ocean—without taking into account ocean wave coastal reflections. Ardhuin *et al.* (2011) introduced the coastal reflection in the wave model. They showed that seismic noise spectra can be modelled with great accuracy and presented the first global maps of noise sources. Stutzmann *et al.* (2012) further showed the seasonal variations of noise source location. The coastal reflection coefficient is not well constrained and should be adjusted as a function of the coast shape (Ardhuin & Roland 2012). Stutzmann *et al.* (2012) provided empirical coastal reflection coefficients for stations in various environments and showed, in agreement with Longuet–Higgins 50 yr earlier, that the strongest noise sources are in deep ocean and that coastal reflection generates numerous smaller sources. The theory was extended to body wave solution by Ardhuin & Herbers (2013).

Previous modelling of seismic noise (Kedar *et al.* 2008; Webb 1992; Ardhuin *et al.* 2011; Stutzmann *et al.* 2012) used the Longuet–Higgins excitation coefficients which correspond to a flat two layers medium at the source. Here, we model seismic noise by normal mode summation in a more realistic spherical earth model and we show that we can reproduce the main features of noise spectra by modelling the sources as vertical single forces and taking into account the bathymetry. The source excitation due to the bathymetry in our realistic model is compared to Longuet–Higgins' results. Attenuation is not well known in the period band of the secondary microseisms. We present an apparent attenuation model that enables us to compute synthetic noise spectra which fit the real spectra with high accuracy in the period band of 4–10 s. We then investigate the effect of the fundamental mode and higher modes on the vertical component of noise spectra. We observe a discrepancy between real and modelled spectra of the horizontal components which can be explained by the existence of Love waves which cannot be generated by vertical forces. Finally, we show that the seasonal variations of noise sources depend on the period and we show the contribution of the different oceans on noise spectra for a station.

2 THEORY

2.1 Deriving force field from the ocean wave model

Seismic noise is generated by the interaction of ocean waves of similar frequencies and nearly opposite directions. Hasselmann (1963) showed how to compute the corresponding pressure field. We use it to derive the analytical expression of the equivalent vertical force field at the ocean surface. The spectral density of the equivalent pressure at the surface of the ocean can be written (Ardhuin *et al.* 2011; Stutzmann *et al.* 2012),

$$F_p(\mathbf{K} \simeq 0,\, f_2 = 2f) = \rho_w^2 g^2 f_2 E^2(f) \times \int_0^{\pi} M(f,\theta) M(f,\theta+\pi) \mathrm{d}\theta \qquad (1)$$

where ρ_w is the water density, g is the gravity acceleration, f_2 is the pressure field frequency and $\mathbf{K}$ is the sum of the wavenumbers of the two opposite ocean waves. $E(f)$ is the surface elevation variance of two wave trains and $M(f, \theta)$ is the non-dimensional ocean wave energy distribution as a function of ocean wave frequency f and azimuth θ. The unit of the surface elevation variance $E(f)$ is $\frac{m^2}{Hz}$, whereas the spectral density F_p is in $\frac{N^2}{m^2 \cdot Hz}$. The integral in eq. (1) depends only on the azimuthal distribution of the ocean wave energy. To simplify the notation we call this non-dimensional integral $I(f)$.

For seismic wavenumbers $\mathbf{K} = (K_x, K_y)$ of magnitude much smaller than a typical wavenumber k of the ocean wave, the pressure power spectrum $F_p(\mathbf{K}, f_2)$ is approximately independent of $\mathbf{K}$. Thus, in the limit $K \ll k$, the surface pressure field for a frequency interval $\mathrm{d}f_2$ and over an area $\mathrm{d}A = R^2 \sin(\Phi')\mathrm{d}\lambda'\mathrm{d}\phi'$—where R is the radius of the Earth, ϕ' is the colatitude and λ' is the longitude—has the same power spectrum as the one caused by a single localized force with a root mean square value

$$F_{\mathrm{rms}}(f_2, \mathrm{d}A, \mathrm{d}f_2) = 2\pi \sqrt{F_p(\mathbf{K} \simeq 0,\, f_2)\mathrm{d}A\mathrm{d}f_2}, \qquad (2)$$

as given by Hasselmann (1963, after eq. 1.17). This equality of the two spectra, the one given by eq. (1) and the one associated to a point force in the middle of a square having length side L and area $\mathrm{d}A = L^2$ can be seen by taking a finite pressure distribution over a small square of area $4a^2$, that is, $p(x, y) = p_0$ for $|x| < a$ and $|y| < a$ and $p(x, t) = 0$ otherwise. If the small square has length side $a < L/2$, the single-sided power spectrum evaluated over the full square is

$$F_{p,a,L}(\mathbf{K}, f_2) = 2p_0^2 \frac{\sin^2(K_x a)}{K_x a} \frac{\sin^2(K_y a)}{K_y a} \left(\frac{4a^2}{2\pi L}\right)^2, \qquad (3)$$

with a value $2p_0^2[4a^2/(2\pi L)]^2$ for $\mathbf{K} \simeq 0$. Thus, the same spectral density as eq. (1) at $\mathbf{K} \simeq 0$ is obtained by setting $p_0 = 2\pi L/(4a^2)$. Since the force is $4a^2 p_0$, it is independent of a and we find eq. (2), which only applies to finite values of K in the limit when a goes to zero, which corresponds to a point force. The same is true for any spatial distribution, for example, taking a Gaussian pressure distribution instead of a constant.

Similarly in the time dimension, the random wave-induced pressure is equivalent to a temporal variation of the force F that will have the same frequency power spectrum as given by eq. (1). In practice, our model is formulated in time domain. We obtain a time-series of the force that has the required power spectrum by summing different frequencies for which we specify an amplitude and a phase. The phase is drawn randomly between 0 and 2π and the amplitude is normalized to be

$$F(f_2) = \sqrt{2} F_{\mathrm{rms}}(f_2, \mathrm{d}A, \mathrm{d}f_2), \qquad (4)$$

so that the variance of the force is indeed $F^2_{\mathrm{rms}}(f_2, \mathrm{d}A, \mathrm{d}f_2)$, with a power spectrum that will thus equal the wave-induced pressure power spectrum given by eq. (1).

To compute the force amplitude we need the spectral density of the equivalent pressure (eq. 1) just below the ocean surface everywhere in the ocean. We use the ocean wave model of Ardhuin *et al.* (2011). The global ocean wave model has a constant resolution

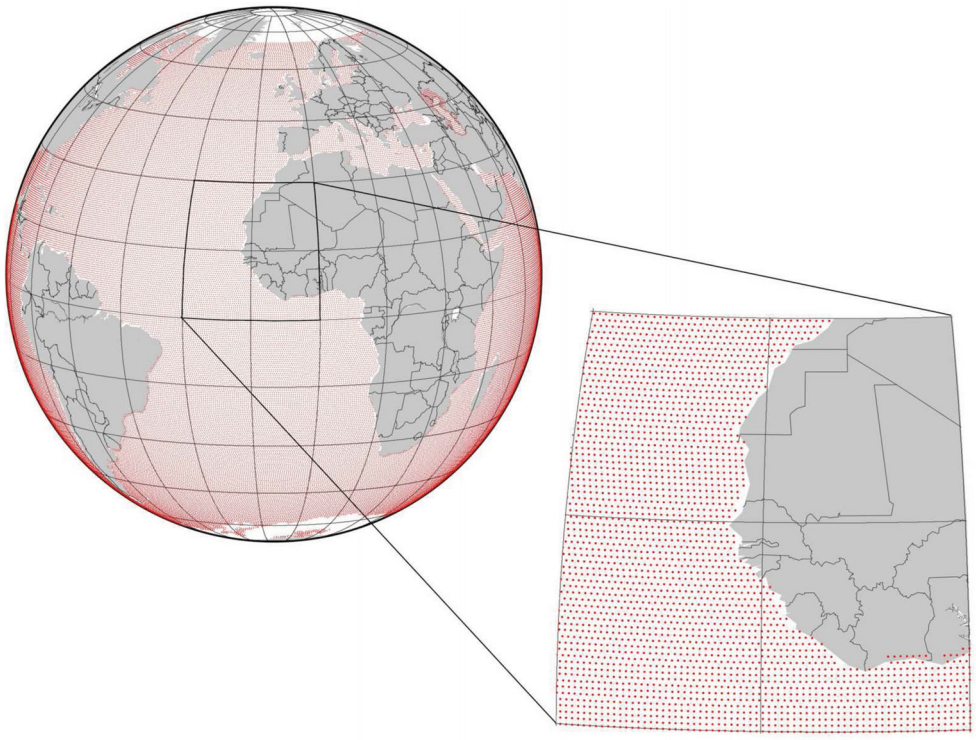

Figure 1. Spherical grid of noise point sources. All the ocean is discretized with a step of 50 km. This represents a good compromise between solution convergence and calculation time.

of 0.5° both in latitude and in longitude. At each gridpoint, the ocean state is described by 24 azimuths and 16 frequencies spaced exponentially between 0.04 Hz ($T = 24.4$ s) and 0.17 Hz ($T = 5.8$ s). One key point of this model is that it is the only model to date which takes into account coastal reflection of ocean waves. We compute the spectral density with and without coastal reflections for performing a linear combination of the two resulting models to obtain the equivalent pressure maps corresponding to a given coastal reflection coefficient. We use in our modelling the empirical reflection coefficients determined by Stutzmann *et al.* (2012) which are different for different regions.

For a given area, we convert the equivalent pressure maps into vertical forces located just below the ocean surface. The discretization in point sources corresponds to dividing a storm area into squares and considering a force concentrated in a point at the centre of each square. All the oceans are discretized on a grid with a step of 50 km, as shown in Fig. 1. We choose this grid step as a good compromise between solution accuracy and calculation time. We tested that a thinner step does not produce any further constructive interference, meaning that the solution has already reached the convergence. At each gridpoint, the source corresponds to a vertical force $F_{\rm rms}(f_2, \mathrm{d}A, \mathrm{d}f_2)$ with a random phase for each frequency step. These sources are then used for computing synthetic seismograms by normal mode summation.

2.2 Normal mode computation

Following Gilbert (1970) and Gilbert & Dziewonski (1975) we calculate the impulse response of a point source and write the seismic displacement in a spherically symmetric, non-rotating, elastic and isotropic (SNREI) earth model as sum of normal modes

$$\mathbf{s}(\mathbf{x}, t) = \sum_k a_k(t)\mathbf{u}_k(\mathbf{r}), \tag{5}$$

where r is the radial coordinate, $\mathbf{u}_k(\mathbf{r})$ is a normalized eigenfunction of the earth model and $a_k(t)$ is the excitation function of mode k. k encapsulates the notations (q, n, l, m), where q can only take two values, one for spheroidal and the other one for toroidal modes, n is the radial order, l is the angular order and m the azimuthal one. Because of the spherical symmetry of the reference model, eigenfunctions do not depend on the azimuthal order m. We consider an instantaneous point force $\hat{\mathbf{f}}(\mathbf{r}, t) = \mathbf{f}(\mathbf{r})g(t)$, with

$$g(t) = \delta(t) \tag{6}$$

and

$$\mathbf{f}(\mathbf{r}) = F\delta(r - r_{0s}), \tag{7}$$

where r_{0s} is the source position. In this case, eq. (5) can be written as

$$\mathbf{s}(\mathbf{x}, t) = \sum_k \int_{-\infty}^{t} \frac{\sin \omega_k t}{\omega_k}\, \mathrm{d}t \int_{V_E} \mathbf{u}_k^*(r) \cdot \mathbf{f}(\mathbf{r})\, \mathrm{d}V, \tag{8}$$

where $\mathbf{u}_k^*(r)$ is the complex conjugate of $\mathbf{u}_k(r)$.

The Green's functions are obtained from the previous equation setting $\mathbf{F} = 1$. Then, during the normal mode summation we compute the spatial convolution with the force $\mathbf{f}(\mathbf{r})$. We show the analytical expression of the synthetic seismogram computation considering a single forces in Appendix A. The formulation in the appendix can be used to compute synthetic seismograms for forces in any direction. Here we only consider vertical forces.

In practice, summation over k cannot be computed numerically without truncations. Synthetic seismograms are computed only up to a given frequency, which enables to define a maximum angular order $l_{\rm max}$ up to which the sum over l has to be calculated. In that case, the temporal part of eq. (8) is rewritten for allowing sum truncation as in Capdeville (2005). The total displacement is the sum of the synthetic displacement generated by each point source.

The temporal part of each source (eq. 6) is a random signal having variance equal to 1.

The 3-D heterogeneities in the Earth generate focusing and defocusing effects of seismic waves. These 3-D effects cannot be accounted for with the normal mode summation method used on this paper. Although these effects have an important influence on waveforms (e.g. Tape *et al.* 2009, 2010; Fichtner *et al.* 2012), considering seismic energy (in dB) with a rough accuracy as it is done here, we assume these effects to be small and the error made, because of this approximation, does not affect our conclusions.

3 NOISE SOURCES EXCITATION

Longuet-Higgins (1950, 1952) first showed that microseismic energy depends on the ocean wave state and on the bathymetry. Bathymetry produces an excitation effect which is frequency dependent. The excitation factor has been calculated analytically by Longuet-Higgins (1950) considering a flat two layers medium as a function of

$$x = \omega h/\beta, \tag{9}$$

where $\omega = 2\pi f_2$ is the angular frequency of the ocean pressure field at the source, h is the ocean depth and β is the S-wave velocity. This particular combination of frequency and depth in eq. (9) is a common way for describing a standing wave system and looking for its nodes. Longuet–Higgins coefficients have been used to analyse the effect of the bathymetry in all previous studies (e.g. Kedar *et al.* 2008; Ardhuin *et al.* 2011; Hillers *et al.* 2012; Stutzmann *et al.* 2012). Here we compute the effect of bathymetry using normal modes and a more realistic spherically symmetric earth model with varying bathymetry. Comparing Longuet–Higgins' eq. (183) (p. 28, Longuet-Higgins 1950) and the synthetic seismogram computation of Appendix A in case of a vertical force, we obtain the expression of the excitation coefficient computed by normal modes,

$$c_n = \frac{{}_n\mathrm{U}_l(\mathbf{r_r})\,{}_n\mathrm{U}_l(\mathbf{r_s})}{\omega}, \tag{10}$$

where ω is the angular frequency of the seismic noise field and ${}_n\mathrm{U}_l$ is the scalar eigenfunction for a mode with indices (n, l). $\mathbf{r_r}$ and $\mathbf{r_s}$ are related, respectively, to the receiver and source positions. The division by ω produces the alignment of all ocean depth curves and enables to plot them as a unique shape. The eigenfunctions are normalized considering $\int_0^R \rho(r)\,{}_n\mathrm{U}_l{}^2(r) r^2 \mathrm{d}r = 1$, where $\rho(r)$ is the density and R the radius of the Earth.

We compute the excitation coefficients using two different models. The first one is the model used by Longuet-Higgins (1950, p. 29), hereafter called two layers model, and the second model is PREM (Dziewonski & Anderson 1981). We vary the ocean depth from 1 to 10 km, in discrete steps by kilometre, to simulate the bathymetry, reproducing intermediate depths by interpolation. We compute eigenfunctions from 3 to 12 s and we calculate c_n by using eq. (10) for each depth and frequency. Fig. 2(a) shows the coefficients c_n as function of $\omega h/\beta$ for the two layers model and Fig. 2(b) shows the coefficients for PREM. Our normalization is different from that of Longuet–Higgins, but we see on Fig. 2(a) that the shape of the curves is the same. Moreover, the abscissa of the resonant peaks is similar between our computation and Longuet–Higgins' results, meaning that we reproduce the maximum excitation peaks for the same combinations of frequency and ocean depth. Differences in shape between Longuet–Higgins and our excitation coefficients are due to the fact that he considered a flat earth model whereas we perform the computation in a spherical earth model.

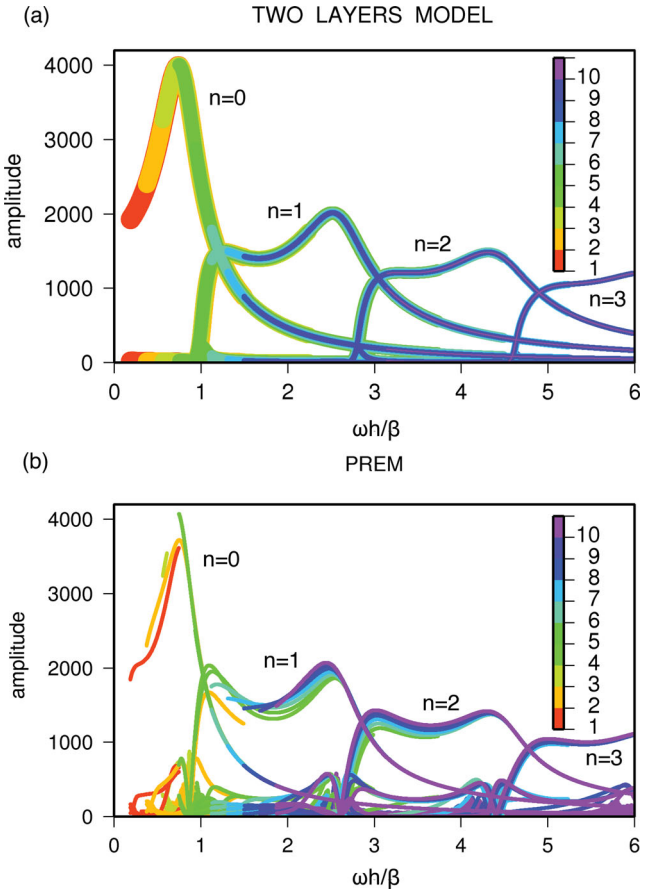

Figure 2. Excitation coefficients due to the bathymetry as computed through our normal mode approach as function of $\omega h/\beta$, where ω is the angular frequency, h is the ocean depth and $\beta = 2800\,\mathrm{m\,s^{-1}}$ is S-wave velocity in the crust. (a) Results obtained for an ocean layer over an half-space, as used in Longuet-Higgins (1950). The vertical point force is located at the top of the ocean layer and the water depth is marked by the colour scale. (b) Same as part (a) but for PREM model. In part (a), we use decreasing thickness for increasing water depth curves to emphasize each ocean depth curve.

Each curve in Figs 2(a) and (b) is related to a given spheroidal mode. The first coefficient ($n = 0$) represents the excitation of the fundamental mode of Rayleigh waves, whereas the others coefficients ($n = 1$, $n = 2$ and so on) are related to the overtones. Our choice of colour scale enables for the first time to understand which modes are excited at any ocean depth. The fundamental mode becomes more and more important for thin ocean layers, whereas for deep oceans, the overtones contribute more to the seismic noise signal.

The curves for PREM (Fig. 2b) have a similar shape with respect to the two layers model ones, with some exceptions. First of all, the different ocean depth curves do not align with each other. This is due to the complexity of the stratified PREM model with respect to a simple ocean layer above an half-space. The first maximum of each curve has an amplitude comparable to the two layers case. Moreover, the amplitude of the first five modes are similar to the two layers case, but this is not the case for the higher overtones. In normal mode language, high-order overtones are related to body waves, meaning that their summation corresponds to the body wave packet. The sum of all modes, computed for PREM earth model, enables to compute the entire synthetic seismogram, including Rayleigh wave fundamental, higher modes and body waves.

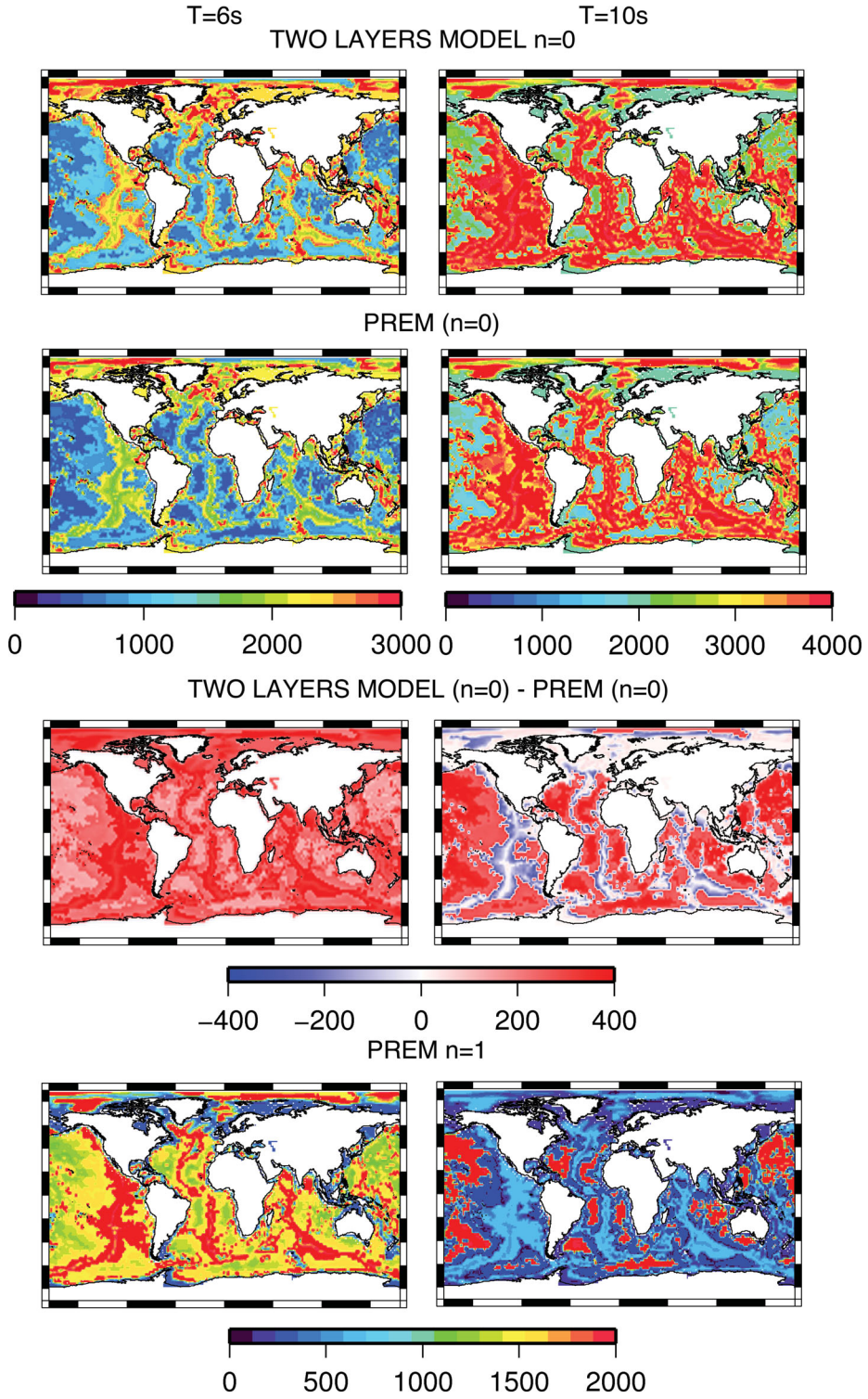

Figure 3. Maps of excitation factor of the fundamental mode $n = 0$ for a fixed period in the two layers model (first row) and PREM model (second row). The third row shows the difference between the coefficients calculated in the two layers model and in PREM. The excitation factors for $n = 1$ are shown in the fourth row. The two columns correspond to 6 s (left) and 10 s (right) of period.

To determine the regions that excites most the surface waves, Fig. 3 shows the excitation coefficients (eq. 10) of the fundamental mode of Rayleigh waves for the two layers model (top row) and the PREM (second row), respectively. These maps are computed for two fixed periods, 6 s (left column) and 10 s (right column) using the same colour scale for a given period. These maps can be compared to those presented by Stutzmann *et al.* (2012) using Longuet–Higgins coefficients. Similarly to their results, we observe that, for a period of 6 s, the most excited regions are in the vicinity of the ridges or at a few hundred kilometres from the coast. Instead, for a period of 10 s, the highest excited area covers most of the oceans, also further away with respect to the ridges. The differences in amplitude between our maps and those by Stutzmann *et al.* (2012) are due to a different normalization.

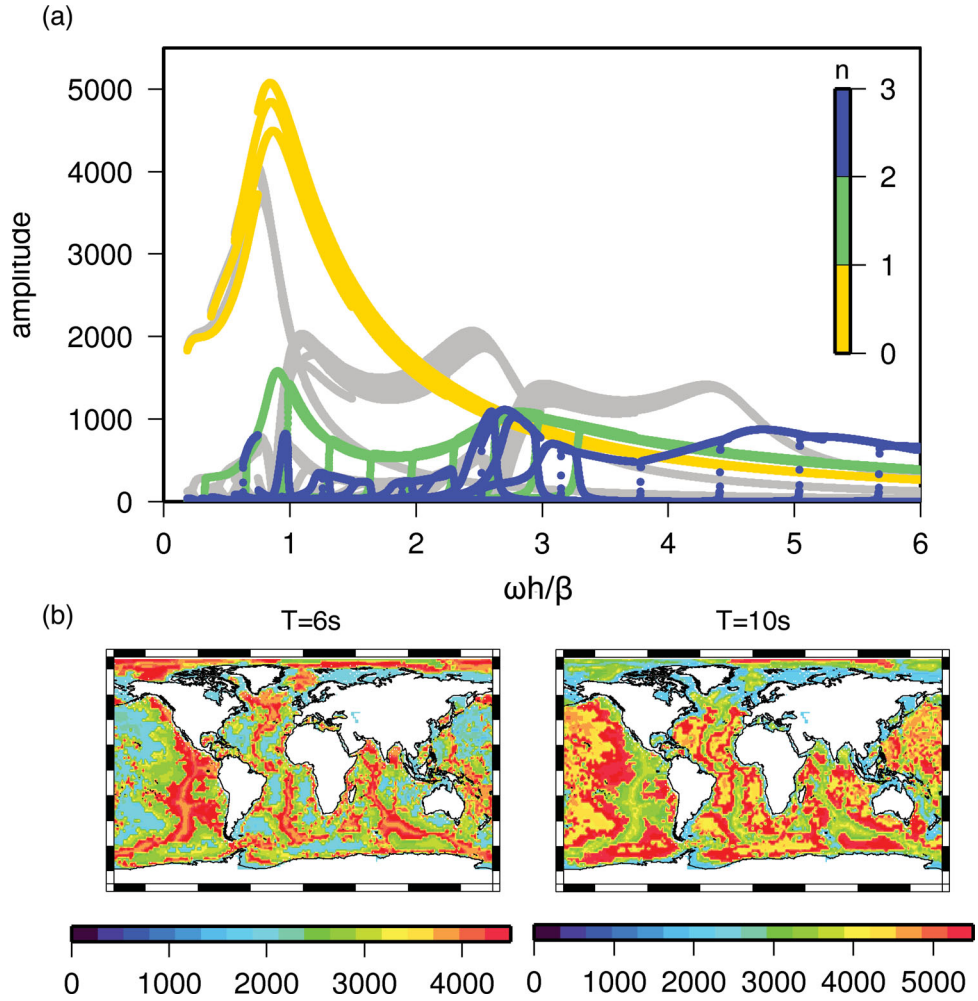

Figure 4. (a) Excitation coefficients due to the bathymetry computed in PREM model as a function of $\omega h/\beta$. ω is the angular frequency, h the ocean depth and $\beta = 2800\,\mathrm{m\,s^{-1}}$ is the S-wave velocity in the crust. We compute them by using eq. (10) and considering eigenfunctions of the oceanic model multiplied by eigenfunctions of the continental model corresponding to the same frequency. In grey, it is shown the case of Fig. 3 with both the eigenfunctions computed in the oceanic model. (b) Maps of the excitation coefficients at 6 and 10 s of period considering oceanic and continental model for computing the eigenfunctions.

The comparison between the excitation coefficient calculated in the two layers model and in PREM (Fig. 3, first two rows) underline the fact that the excitation depends not only on bathymetry but also on the seismic structure below the seafloor. The maxima are at the same locations for the two models but the amplitudes are in general smaller for PREM. The difference between the excitation coefficients calculated in the two layers model and in PREM model (Fig. 3, third row) shows that, for a period of 6 s, the noise sources are more excited in the two layers model with respect to PREM everywhere and particularly on both sides of the ridges. For a period of 10 s, sources in most of the ocean area are also overexcited in the two layers case, except for regions around ridges where sources are underexcited.

We can also compare the excitation coefficients for the fundamental mode $n = 0$ and the most energetic overtone $n = 1$ (Fig. 3 second and last rows), both of them calculated in PREM. The overtone $n = 1$ shows an amplitude of the excitation coefficients smaller than the fundamental mode. The maximum amplitudes are of the same order of magnitude for both 6 and 10 s. We also see that the highest excitation areas are not the same than for the fundamental mode (second row, Fig. 3), especially for the period of 10 s.

The normal mode theory used here assumes a spherically symmetric earth model between source and receiver. When this model has a water layer (like PREM model), the station depth is set at the ocean bottom. Therefore, 3-D Earth feature effects on wave propagation, such as ocean–continent transition, can not be accounted for. To estimate this error and check if it does not significantly affect our conclusions, we compute the excitation coefficients using eq. (10) with eigenfunctions of the oceanic model multiplied by eigenfunctions of the continental model corresponding to the same frequency.

The excitation coefficients of the Rayleigh waves fundamental mode (yellow curve) are broader and higher (Tanimoto 2012) than in our previous modelling (in grey for comparison). We also observe that the overtones (green and blue lines) have much smaller amplitude.

Because we model the amplitude of noise spectra in dB, the difference of the excitation coefficients of the fundamental mode between the two cases is not so strong and it does not affect our final results.

For comparing the spatial sources distribution, Fig. 4(b) shows two maps of the excitation coefficients at 6 and 10 s of period for the fundamental mode computed by using a model without ocean

for one of the eigenfunctions and with ocean for the other. Making a comparison with the second line maps in Fig. 3, we observe the same location of maxima amplitude for 6 s and a different location for 10 s of period.

However, the use of different models for the source and receiver eigenfunction—respectively with and without ocean layer—produces, when we perform normal mode summation, an error linked with the different discretization of the angular order domain. This error increases for short period, where the normal modes catalogue becomes dense.

4 SEISMIC NOISE MODELLING

4.1 Group velocity and attenuation

There is no global attenuation model that is accurate in the period band 3–15 s. Therefore, we started with the QL6 model (Durek and Ekström 1996), valid for long periods ($150 < T < 300$ s), and we modified it in the upper 100 km by decreasing Q. In this way we find out an apparent attenuation model that enables a good fit between data amplitude and synthetic spectra. For depths below 100 km, Q_μ and Q_k remain the same as $QL6$. Decreasing Q, we maintain the ratio between Q_μ and Q_k with respect to $QL6$. Fig. 5 shows Q_μ in $QL6$ (in black) and in our model (in red) for crustal and mantle depths, shallower than 100 km. We note a difference of about 90 per cent between these two models. We calibrate our apparent attenuation model for station SSB and we observe that it is valid also to reproduce data of other stations located in other environments.

In Fig. 6, we show group velocity U and attenuation factor ${}_0q_l$ for the fundamental mode of Rayleigh waves calculated with normal modes for periods from 4 to 10 s (Takeuchi & Saito 1972) considering PREM and varying bathymetry. ${}_0q_l$ corresponds to the inverse of the complex part of the eigenfrequencies ${}_0\omega_l$. We observe in Fig. 6(a) that the attenuation of Rayleigh waves within the Earth increases with decreasing period, as already shown by Pierson &

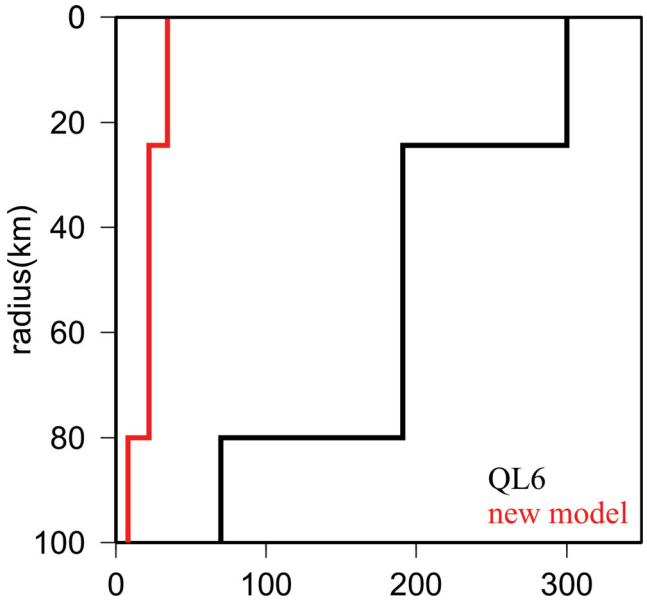

Figure 5. Model of the attenuation parameter Q_μ for periods between 4 and 10 s. In black is shown our starting model $QL6$ (Durek & Ekström 1996) and in red our final apparent attenuation model Q_μ that permits best data fits using normal mode approach.

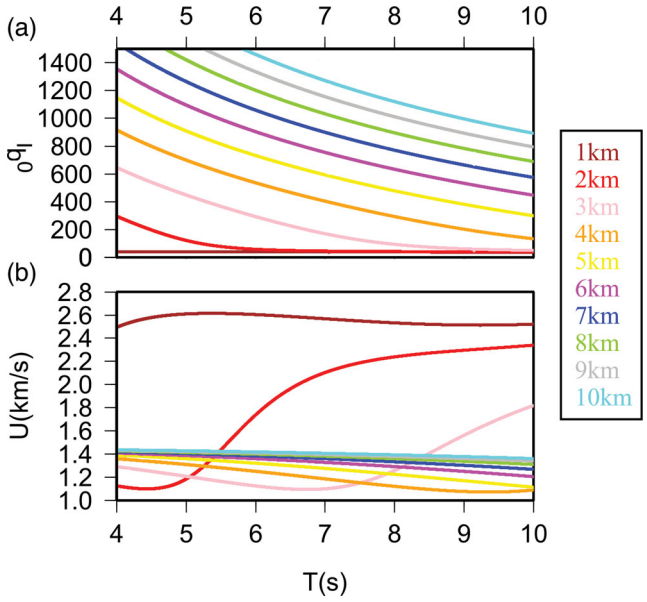

Figure 6. Attenuation factor and group velocity for the fundamental mode Rayleigh waves as function of period between 4 and 10 s. The corresponding normal mode computation follow Takeuchi and Saito (1972). The different colours mark the ocean depths between 1 and 10 km.

Moskowitz (1963), McCreery *et al.* (1993) and Webb (1998). We further show that ${}_0q_l$ is increasing with increasing water depth for the fundamental mode ($n = 0$). The range of ${}_0q_l$ values presented in Fig. 6 are consistent with those obtained by Stutzmann *et al.* (2012) and by Prieto *et al.* (2011) at a local scale.

In Fig. 6(b) we plot the fundamental mode group velocity as a function of period and water depth for PREM. For a water depth of 1 km, group velocity is about 2.5 km s^{-1}. For a water depth of 2 km, we observe a strong variation of group velocity between 1.1 km s^{-1} for a period of 4 s and 2.4 km s^{-1} for a period of 10 s. For larger water depth, group velocities are all between 1.2 to 1.4 km s^{-1} in the entire period range. The varying group velocity as a function of the bathymetry and period is related to the link between the Rayleigh wave wavelength and the thickness of the water layer.

4.2 Vertical component of noise spectra

We compute synthetic noise power spectra using normal mode summation as described in Appendix A. A vertical force F_r is calculated for each gridpoint on the ocean surface. Synthetic spectra are computed using the ocean wave hindcasts of Ardhuin *et al.* (2011) and the coastal reflection coefficients determined by Stutzmann *et al.* (2012).

Fig. 7 displays real and synthetic spectra in dB with respect to the acceleration as function of period for 3 hr of observations at station SSB (France, Geoscope network). The synthetic spectrum is computed for the sum of the first 100 modes (crosses over a black thin line) and for each mode separately. The total synthetic spectrum (100 modes) reproduces well the real spectrum. The comparison between the different modes shows that the fundamental mode is the most energetic in the entire period band and that the synthetic spectrum amplitude decreases with increasing the overtone order. Moreover, the difference between them becomes smaller with increasing the overtone order: we observe a difference of about 40 dB at 8 s between the fundamental mode (yellow line) and the first overtone

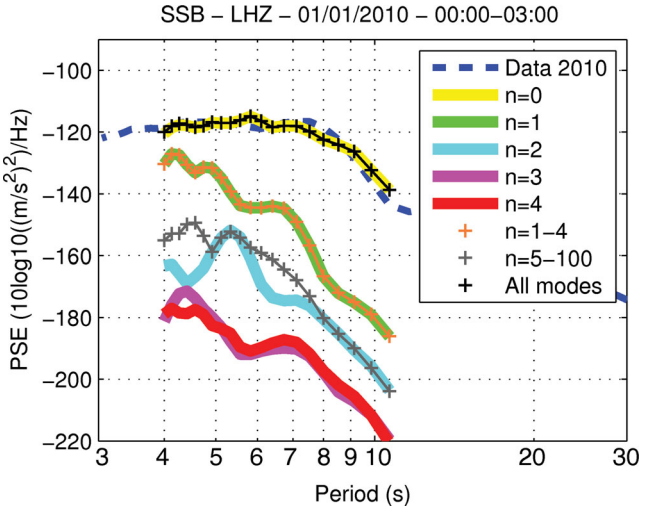

Figure 7. Vertical component of seismic noise spectra in d*B* for 3-hr of observations in station SSB (France). We show the comparison between data (blue dashed line) and synthetic spectra splitting the contribution of fundamental mode and overtones. The amplitude of the synthetic spectra decreases increasing the overtones number.

(green line) and an overlap between the overtones $n = 3$ (magenta line) and $n = 4$ (red line) for the same period. The summation of the first 100 modes (crosses over a black thin line) is superimposed on the spectrum computed with the fundamental mode only, confirming that the fundamental mode of Rayleigh waves is the dominant signal in seismic noise recorded by the vertical component. We also observe that the spectral amplitude computed using only the first overtone has similar amplitude to the spectrum computed with overtones from $n = 1$ to $n = 4$ (crosses over a thin orange line).

Fig. 8 shows the power spectral energy in d*B* with respect to the acceleration as a function of period for the vertical component of three Geoscope continental stations, SSB in France (Fig. 8b), TAM in Algeria (Fig. 8c) and CAN in Australia (Fig. 8d). Seismic spectra are averaged over the year 2010. Data are shown in blue and the corresponding synthetic spectra in black. Synthetic seismograms are calculated between 4 and 10 s. Coastal reflection coefficients are taken from Stutzmann *et al.* (2012) for each station: 2 per cent for SSB, 2 per cent for TAM and 6 per cent for CAN. The synthetic spectra reproduce quite well both amplitude and shape of the real spectra for all stations. We recall that these three spectra, related to stations respectively in Europe, Africa and Oceania, have been calculated using the same attenuation model, described in the previous section and plotted in Fig. 6. In this way, we validate our attenuation model for the the secondary microseismic period band.

4.3 Horizontal components of noise spectra

A vertical point force applied on a locally flat seafloor does not generate Love waves. Rayleigh waves instead show energy on the vertical and the two horizontal components of the receiver. As we consider here only vertical forces, we model only Rayleigh waves and body waves on the three components. Then, the discrepancy between real and synthetic spectra on the horizontal components can be used to estimate the amount of Love waves present in the noise. Fig. 9 shows noise spectra for the East (a) and North (b) components of the Algerian station TAM. Noise spectra are averaged over the year 2010. We observe a discrepancy between the synthetic and real spectra which is varying with frequency and is about 10 d*B* at 7 s of period.

Nishida *et al.* (2008) showed evidence of Love waves in seismic noise spectra also in the secondary microseismic period band. Saito (2010) and Fukao *et al.* (2010) developed a theory of Love-wave generation based on the fact that a vertical force applied on a bathymetric shape with a non-null gradient can be separated into a horizontal and a vertical component. The horizontal component then excites Love waves and the vertical generates Rayleigh waves.

We make the hypotheses that the discrepancy between real and synthetic spectra is dominantly due to the presence of Love waves in recorded signal. Nishida *et al.* (2008), in their Fig. 2(c), calculated the kinetic energy ratio between Rayleigh and Love. Considering only periods between 4 and 10 s, this ratio takes value between 0.5 and 0.7, meaning that Love waves have a kinetic energy varying between 50 and 70 per cent with respect to Rayleigh wave kinetic energy. Considering, for example, a period of 7 s, we can write a relation between the square velocities: $v_L^2 \sim 0.65\ v_R^2$. Adding to the energy of Rayleigh waves (black line in Fig. 9) the energy of Love waves calculated from this ratio, we obtain analytically PSE $= -134.89$ d*B* for a period of 7 s, which is approximately the amplitude of the real spectra in Fig. 9 (blue dashed line). Doing this simple analytical computation, we find a proportion of Love waves energy in agreement with Nishida *et al.* (2008). Modelling Love waves is beyond the scope of this paper but it can easily be done with normal mode theory as shown in Appendix A, considering additional horizontal forces or the components factorization of vertical forces when they are applied on a bathymetry having a non-null gradient.

4.4 Seasonal variations

Fig. 10 shows background noise seasonal variations for seismic station TAM. Schimmel *et al.* (2011a,b) and Stutzmann *et al.* (2012) analysed noise polarization and concluded that this station records noise coming from all surrounding oceans: Atlantic, Indian and Mediterranean Sea. Here, we quantitatively investigate the contribution on noise spectrum amplitude of noise sources located in each ocean. We divide the Atlantic Ocean in two parts, at the Equator, to show their influence separately. We calculate average synthetic spectra for each month of year 2010. In Fig. 10 we show four cases: 2010 January, April, July and December. With blue dashed line we represent data and with crosses over a thin black line our synthetics. We plot on the same figure four other coloured lines, which represent the contribution of the different portions of the surrounding oceans on spectra amplitude. Coloured lines correspond to the coloured oceans in the map.

In January (Fig. 10a), the strongest contribution comes from the Northern Atlantic Ocean (green line) and it is sufficient to reproduce the real spectrum. The Southern Atlantic Ocean (red line) and the Indian Ocean (magenta line) generate noise spectra of similar magnitude within $\sim$5 d*B*, the first one being larger above 7 s of period and the second one being larger below 7 s of period. This suggests the existence of bigger storms in the Southern Atlantic than in the Indian Ocean. But, both spectra are $\sim$20 d*B* smaller than the Northern Atlantic Ocean spectrum. The contribution due to the Mediterranean Sea (yellow line) is really small for periods longer than 6 s. This is related to the smaller size of the Mediterranean Sea with respect to the oceans which limits the size of the storms and therefore the maximum period of the ocean waves. At very short period—4 and 5 s—the role played by the Mediterranean Sea becomes comparable to the contribution of Southern Atlantic

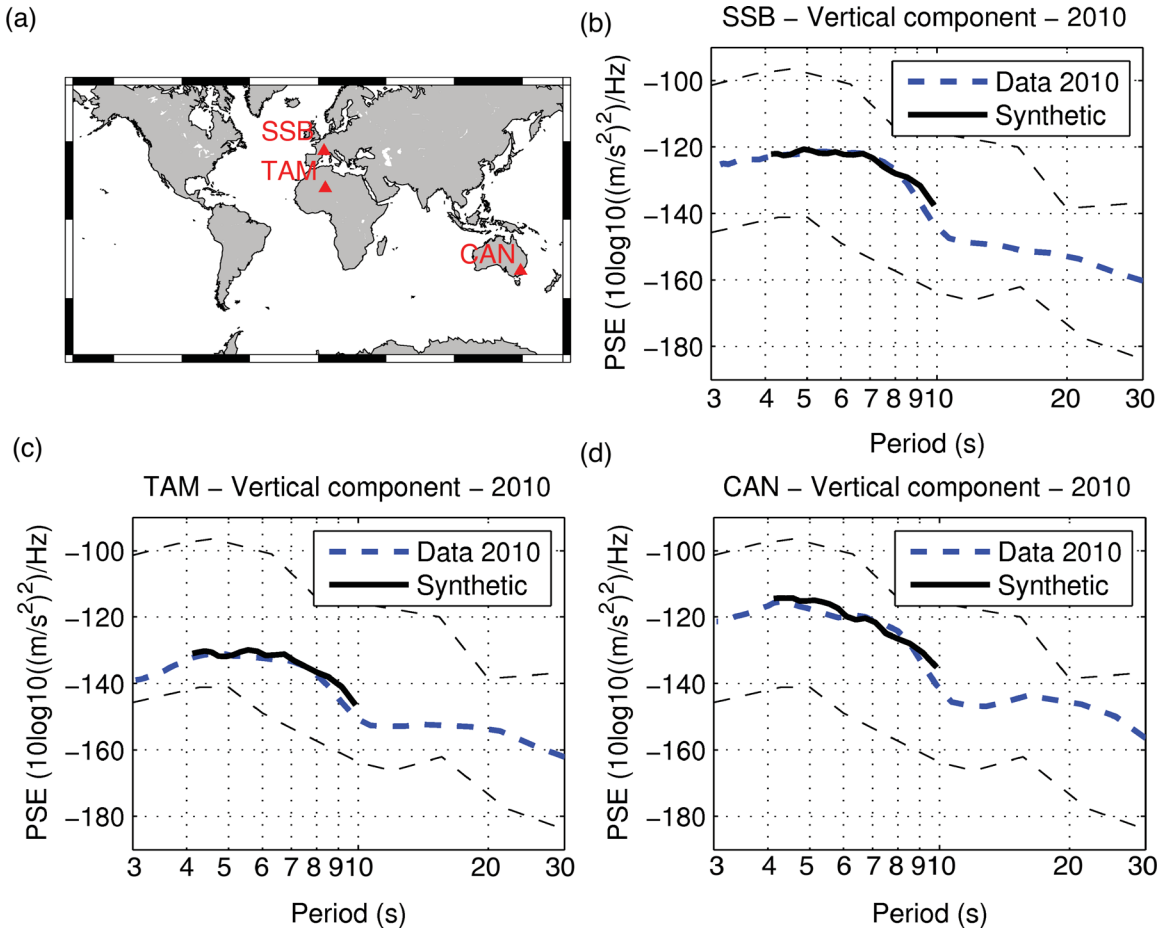

Figure 8. (a) Map with used seismic stations. (b) Vertical component noise spectra in dB for SSB (France). (c) Vertical component noise spectra in dB for TAM (Algeria). (d) Vertical component noise spectra in dB for CAN (Australia). All seismic spectra are averaged over the year 2010. Data are shown in blue and the corresponding synthetic spectra in black. The period range of interest is between 4 and 10 s. Synthetic spectra are computed with the IOWAGA ocean wave model using the same attenuation profiles as function of ocean depth and frequency. Dashed black lines represent respectively the low-noise model (LNM) and the high-noise model (HNM) spectra (Peterson 1993).

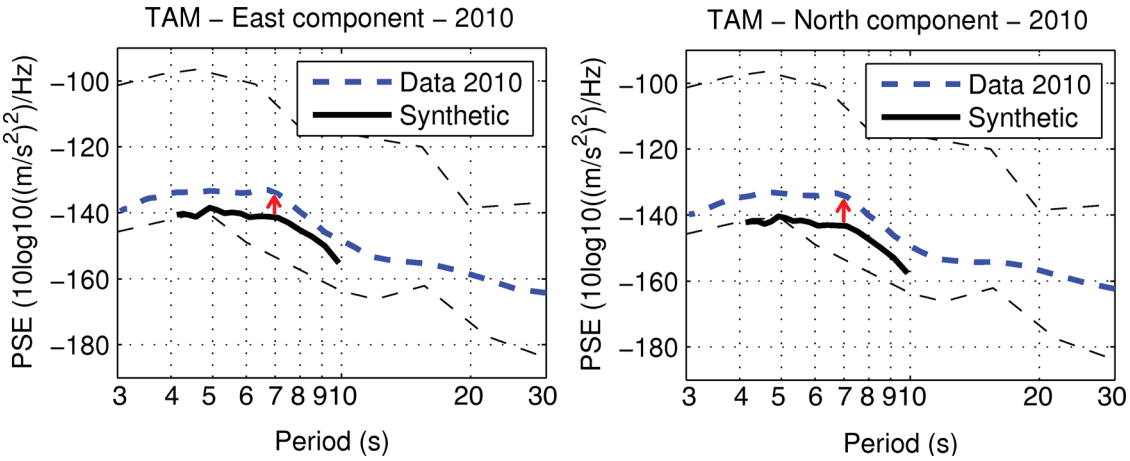

Figure 9. Horizontal components of noise seismic spectra in dB for station TAM. Panel (a) shows the East component and panel (b) the North component. The difference between theoretical and data spectra is ascribed to the unmodelled Love wave energy inherent to our computation where we use vertical point forces and a locally flat seafloor. Under this assumption, the estimated Rayleigh wave to Love wave energy ratio is consistent with Nishida *et al.* (2008). Dashed black lines represent respectively the low-noise model (LNM) and the high-noise model (HNM) spectra (Peterson 1993).

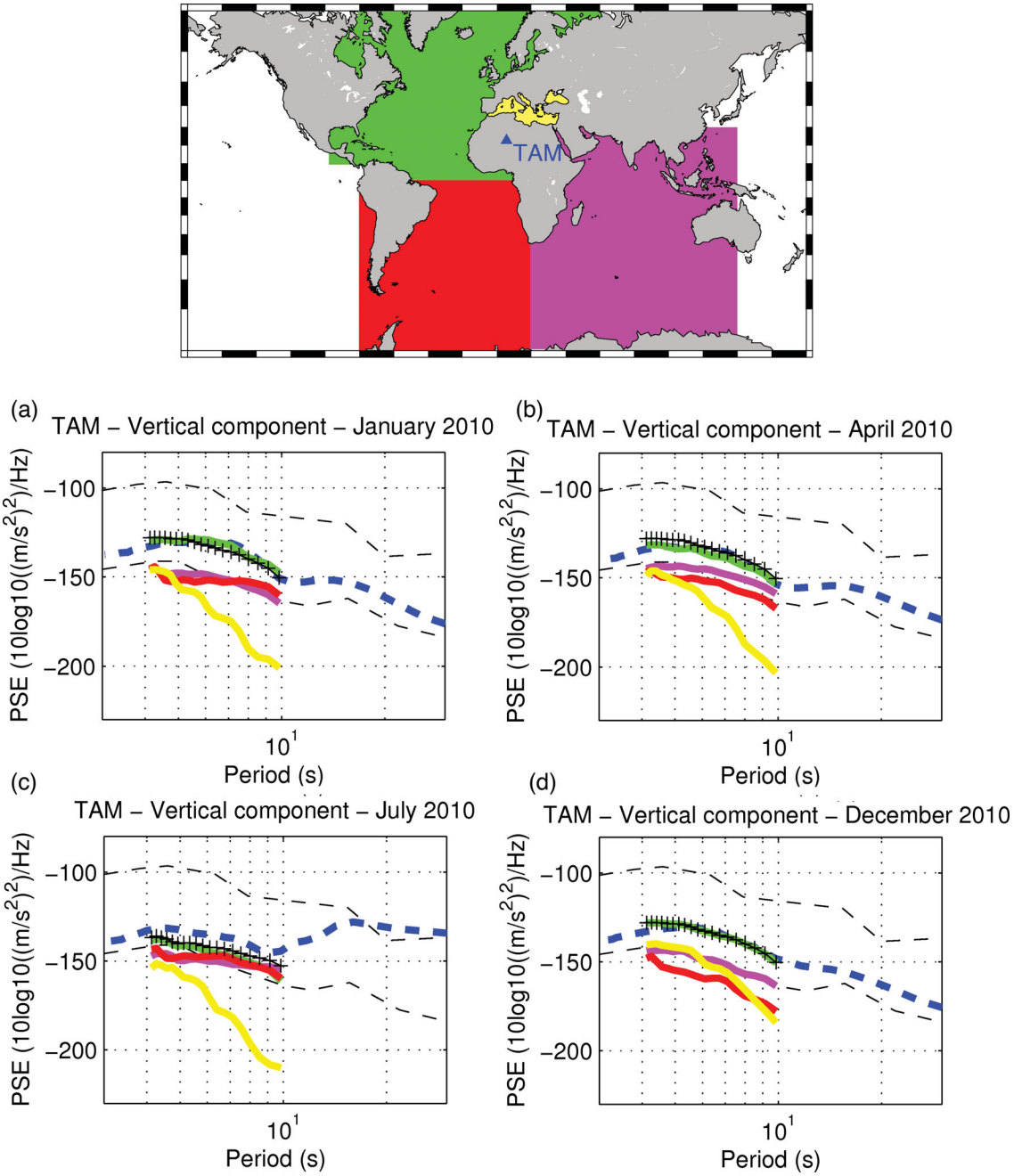

Figure 10. Seasonal variations of vertical component of seismic noise spectra for station TAM. Shown are the real (blue dashed line) and synthetic (crosses over a thin black line) data spectra for (a) January, (b) April, (c) July and (d) December 2010. Coloured lines mark the contribution due to different portions of the ocean (map above). We observe that, for station TAM, the Northern Atlantic Ocean produces the main contribution in terms of noise source amplitude almost all the year. Interesting is the increasing noise level in December due to the Mediterranean Sea at short periods. Dashed black lines represent respectively the low-noise model (LNM) and the high-noise model (HNM) spectra (Peterson 1993).

Ocean and Indian Ocean, whereas at long periods the corresponding spectrum is 40 d*B* smaller.

In April 2010 (Fig. 10b), the spectrum corresponding to the Northern Atlantic Ocean activity dominates and fits well the observed average spectrum. The spectrum generated by the Mediterranean Sea sources has almost the same shape as in 2012 January with a significant contribution only for short periods. The spectrum generated by sources in the Indian Ocean is ∼10 d*B* smaller than the real spectrum, and that generated by South Atlantic sources is ∼15 d*B* smaller than the real spectrum.

During summer (Fig. 10c), we observe a different pattern. Northern Atlantic Ocean remains the strongest source area, but only for periods below 6 s. At longer period, the energy amount coming from the Southern Atlantic Ocean, the Indian Ocean and the North Atlantic similarly contribute to the total noise spectrum. This is due to the fact that during the boreal summer the strongest seismic noise sources are located on the southern hemisphere (e.g. Stutzmann *et al.* 2012). Southern hemisphere sources are stronger but they are further away that the sources in the North Atlantic Ocean and therefore, they all contribute to the total spectrum. Mediterranean Sea

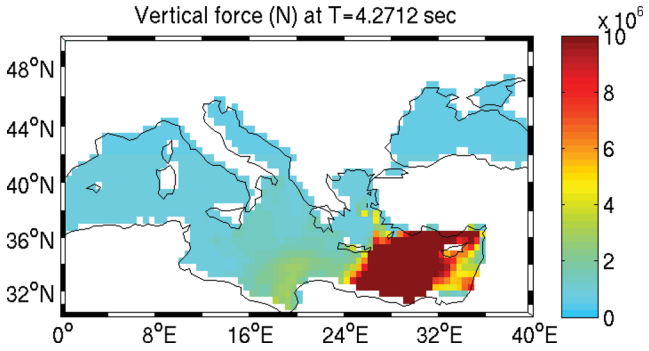

Figure 11. Vertical force as averaged over 2010 December in the Mediterranean Sea for a fixed period of ∼4.3 s. The red patch near Turkey and Egypt is related to storm activity and it is the responsible of the increasing noise level at short periods due to that area (Fig. 10d).

contribution is small and the corresponding spectrum is between ∼10 dB and ∼20 dB below the real spectrum.

Finally in December (Fig. 10d), the Northern Atlantic Ocean sources give again a dominant contribution to the spectra as expected during the northern hemisphere winter. Indian Ocean and Southern Atlantic Ocean contributions are again smaller with a bigger contribution of Indian Ocean of about 10 dB for most frequencies. The interesting feature of this month is related to the Mediterranean Sea. The corresponding spectrum for period shorter than 8 s becomes 20 dB larger than the other months and larger than the spectra corresponding to the Southern Atlantic Ocean and Indian Ocean by up to 10 dB. This is due to a strong storm activity in the Mediterranean sea. Fig. 11 shows, for a period of ∼4 s, the corresponding source area that is located near Turkey and Egypt. We have plotted here the vertical force derived from the ocean wave model as average over 2012 December.

5 CONCLUSIONS

In this paper, we present the theory for modelling the secondary microseisms by normal mode summation. We show that the noise sources can be modelled by vertical forces and how to derive them from a realistic ocean wave model that takes into account coastal reflection. We discretize the oceans and we sum up the contribution of all sources. Bathymetry is an important parameter because it modulates the excitation of the seismic waves. We show how to compute bathymetry excitation effects in a realistic earth model using normal modes and we compare our results with Longuet-Higgins (1950) computation for a two layers flat model. We show that, compared to our more realistic case, the two layers model over predicts the fundamental mode excitation at 6 s of period and that at longer periods, the two layers model either overpredicts or underpredicts the excitation depending on the area. We also show that strongest excitation areas depend not only on the bathymetry and period, but also on the seismic mode.

Seismic noise is then modelled by normal mode summation considering varying bathymetry. We derive an attenuation model than enables to fit well the vertical component spectra whatever the station location. We select three stations in three different continents and we show the good agreement between data and synthetic spectra, both in amplitude and in shape, reproducing all the frequency content of the secondary microseismic noise peak. We show that the fundamental mode of Rayleigh wave is the dominant signal in seismic noise.

We present the first modelling of noise on the horizontal components. We consider noise sources as vertical forces and a vertical point force applied on a locally flat seafloor does not generate Love waves but they generate Rayleigh and body waves on the vertical and the two horizontal components. We use the discrepancy between the real and synthetic spectra of the horizontal components to estimate the amount of missing Love waves in our synthetic spectra. Our estimation is in agreement with Nishida *et al.* (2008). Modelling Love waves is beyond the scope of this paper but it will be done in the future with the normal mode theory of Appendix A, considering additional horizontal forces or the components factorization of vertical forces related to the topography of the bathymetry.

We quantify the influence of noise sources in the different oceans recorded by the station TAM in Algeria. We confirm that this station records noise sources from all surrounding oceans and we study separately the contributions of the different portions of the ocean. We show that the Northern Atlantic Ocean remains all the time the main noise sources area. Nevertheless, we show that the Mediterranean Sea also can contribute significantly to the short period noise in winter.

The modelling as presented here can be directly used to investigate in details the Rayleigh wave and body waves generation. The formalism presented in the Appendix can be used to investigate the generation of Love waves in relation with the topography of the ocean bottom. Finally, this formalism is well adapted for modelling the hum considering appropriate sources.

ACKNOWLEDGEMENTS

We thank the support from the QUEST Initial Training network founded within the EU Marie Curie Program. M.S. acknowledges support by ILink2010-0112. Most of the figures were realized using Generic Mapping Tools (GMT; Wessel & Smith 1998). This is IPGP contribution number 3386.

REFERENCES

Aki, K. & Richards, P.G., 2002. *Quantitative seismology*, 2nd edn, University Science Books, Sausalito, California.

Ardhuin, F., Stutzmann, E., Schimmel, M. & Mangeney, A., 2011. Ocean wave sources of seismic noise, *J. geophys. Res.*, **116,** C09004, doi:10.1029/2011JC006952.

Ardhuin, F., Balanche, A., Stutzmann, E. & Obrebski, M., 2012. From seismic noise to ocean wave parameters: general methods and validation, *J. geophys. Res.*, **117,** C05002, doi:10.1029/2011JC007449.

Ardhuin, F. & Roland, A., 2012. Coastal wave reflection, directional spread, and seismoacoustic noise sources, *J. geophys. Res.*, **117,** C00J20, doi:10.1029/2011JC007832.

Ardhuin, F. & Herbers, T.H.C., 2013. Noise generation in the solid Earth, oceans and atmosphere, from nonlinear interacting surface gravity waves in finite depth, *J. Fluid Mech.,* **716,** 316–348.

Berger, J., Davis, P. & Ekstrm, G., 2004. Ambient earth noise: a survey of the global seismographic network, *J. geophys. Res.*, **109,** B11307, doi:10.1029/2004JB003408.

Bromirski, P. & Duennebier, F., 2002. The near-coastal microseism spectrum: spatial and temporal wave climate relationships, *J. geophys. Res.*, **107**(B8), ESE 5-1–ESE 5-20.

Capdeville, Y., 2005. An efficient Born normal mode method to compute sensitivity kernels and synthetic seismograms in the Earth, *Geophys. J. Int.*, **163,** 639–646.

Cessaro, R.K., 1994. Sources of primary and secondary microseisms, *Bull. seism. Soc. Am.*, **84**(1), 142–148.

Chevrot, S., Sylvander, M., Ponsolles, C., Benahmed, S., Lefevre, J.M. & Paradis, D., 2007. Source locations of secondary microseisms in western

Europe: evidence for both coastal and pelagic sources, *J. geophys. Res.*, **112,** B11301, doi:10.1029/2007JB005059.
Durek, J.J. & Ekström, G., 1996. A radial model of anelasticity consistent with long-period surface-wave attenuation, *Bull. seism. Soc. Am.*, **86**(1A), 144–158.
Dziewonski, A. & Anderson, D., 1981. Preliminary reference earth model, *Phys. Earth planet Inter.*, **25,** 297–356.
Fichtner, A., Trampert, J., Cupillard, P., Saygin, E., Taymaz, T. & Villasenor., A., 2012. Imaging the North Anatolian Fault Zone with multi-scale full waveform inversion, Fall Meeting Abstract 1457037, AGU, San Francisco, CA.
Friedrich, A., Kruger, F. & Klinge, K., 1998. Ocean-generated microseismic noise located with the Grafenberg array, *J. Seismol.*, **2,** 47–64.
Fukao, Y., Nishida, K. & Kobayashi, N., 2010. Seafloor topography, ocean infragravity waves, and background Love and Rayleigh waves, *J. geophys. Res.*, **115,** B04302, doi:10.1029/2009JB006678.
Gilbert, F., 1970. Excitation of the normal modes of the Earth by earthquake sources, *Geophys. J. R. astr. Soc.*, **22,** 223–226.
Gilbert, F. & Dziewonki, A.M., 1975. An application of normal mode theory to the retrieval of structural parameters and source mechanisms from seismic spectra, *Phil. Trans. R. Soc.*, **278**(A278), 187–269.
Gerstoft, P. & Tanimoto, T., 2007. A year of microseisms in southern California, *Geophys. Res. Lett.*, **34,** L20304, doi:10.1029/2007GL031091.
Hasselmann, K., 1963. A statistical analysis of the generation of microseisms, *Rev. Geophys.*, **1,** 177–209.
Haubrich, R. & McCamy, K., 1969. Microseisms: coastal and pelagic sources, *Rev. Geophys.*, **7,** 539–571.
Hillers, G., Graham, N., Campillo, M., Kedar, S., Landes, M. & Shapiro, N., 2012. Global oceanic microsoism sources as seen by seismic arrays and predicted by wave action models, *Geochem. Geophys. Geosyst.*, **13,** Q01021, doi:10.1029/2011GC003875.
Kedar, S., Longuet-Higgins, M., Graham, F.W.N., Clayton, R. & Jones, C., 2008. The origin of the deep ocean microseisms in the North Atlantic Ocean, *Proc. R. Soc. Lond. Ser. A.*, **464**(2091), 777–793.
Longuet-Higgins, M.S., 1950. A theory of the origin of microseisms, *Phil. Trans. Roy. Soc.*, **243**(857), 1–35.
Longuet-Higgins, M.S., 1952, Can sea waves cause microseisms?, in *Proceedings of the Symposium on Microseisms*, U.S. Natl. Acad. Sci. Publ., Vol. 306, pp. 74–93.
McCreery, C., Duennebier, F. & Sutton, G., 1993. Correlation of deep ocean noise (0.4-20Hz) with wind, and the holu spectrum, a world-wide constant, *J. acoust. Soc. Am.*, **93**(5), 2639–2648.
Miche, A., 1944. Mouvements ondulatoires de la mer an profondeur croissante ou dècroissante. Première partie. Mouvements ondulatoires pèriodiques et cylindriques en profondeur constante, *Annales des Ponts at Chaussès*, **114,** 42–78.
Nishida, K., Kawakatsu, H., Fukao, Y. & Obara, K., 2008. Background Love and Rayleigh waves simultaneously generated at the Pacific Ocean floors, *Geophys. Res. Lett.*, **35,** L16307, doi:10.1029/2008GL034753.
Obrebski, M.J., Ardhuin, F., Stutzmann, E. & Schimmel, M., 2012. How moderate sea states can generate loud seismic noise in the deep ocean, *Geophys. Res. Lett.*, **39,** L11601, doi:10.1029/2012GL051896.
Peterson, J., 1993. Observations and modeling of seismic background noise, USGS Open-File Report 93-322, pp. 95.
Phinney, R.A. & Burridge, R., 1973. Representation of the elastic-gravitational excitation of a spherical earth model by generalized spherical harmonics, *Geophys. J. R. astr. Soc.*, **34,** 451–487.
Pierson, W. & Moskowitz, L., 1963. A proposal spectral for fully developed wind seas based on the similarity theory of s.a. kiaigorodskii, *J. geophys. Res.*, **69,** 5181–5190.
Prieto, G.A., Denolle, M., Lawrence, J.F. & Beroza, G.C., 2011. On amplitude information carried by the ambient seismic field, *Phys. Earth Int.*, **343,** 600–614.
Saito, T., 2010. Love-wave excitation due to the interaction between a propagating ocean wave and the sea-bottom topography, *Geophys. J. Int.*, **182,** 1515–1523.
Schulte-Pelkum, V., Earle, P. & Vernon, F., 2004. Strong directivity of ocean-generated seismic noise, *Geochem. Geophys. Geosyst.*, **5,** Q03004, doi:10.1029/2003GC000520/.
Schimmel, M., Stutzmann, E., Ardhuin, F. & Gallart, J., 2011a, Earth's ambient microseismic noise, *Geochem. Geophys. Geosyst.*, **12,** Q07014, doi:10.1029/2011GC003661.
Schimmel, M., Stutzmann, E. & Gallart, J., 2011b. Using instantaneous phase coherence for signal extraction from ambient noise data at a local to a global scale, *Geophys. J. Int.*, **184,** 494–506.
Stehly, L., Campillo, M. & Shapiro, N., 2006. A study of the noise from its long-range correlation properties, *J. geophys. Res.*, **111,** B10306, doi:10.1029/2005JB004237.
Stutzmann, E., Roult, G. & Astiz, L., 2000. Geoscope station noise level, *Bull. seism. Soc. Am.*, **90,** 690–701.
Stutzmann, E., Ardhuin, F., Schimmel, M., Mangeney, A. & Patau, G, 2012. Modeling long-term seismic noise in various environments, *Geophys. J. Int.*, **191**(2), 707–722.
Takeuchi, H. & Saito, M., 1972. Seismic surface waves, *Methods Comput. Phys.*, **11,** 217–295.
Tanimoto, T., 2012. Seismic noise generation by ocean waves: views from normal-mode theory, Fall Meeting Abstract 1487125, AGU, San Francisco, CA.
Tape, C., Liu, Q., Maggi, A. & Tromp, J., 2009. Adjoint tomography of the southern California crust, *Science*, **325**(5943), 988–992.
Tape, C., Liu, Q., Maggi, A. & Tromp, J., 2010. Seismic tomography of the southern California crust based on spectral-element and adjoint methods, *Geophys. J. Int.*, **180,** 433–462.
Webb, S.C., 1992. The equilibrium oceanic microseism spectrum, *J. acoust. Soc. Am.*, **92**(4), 2141–2158.
Webb, S., 1998. Broadband seismology and noise under the ocean, *Rev. Geophys.*, **36,** 105–142.
Wessel, P. & Smith, W.H.F., 1998. New improved version of the Generic Mapping Tools released, *EOS Trans. Am. geophys. Un.*, **79**(47), 579.
Woodhouse, J.H. & Girnius, T.P., 1982, Surface waves and free oscillations in a regionalized earth model, *Geophys. J. E. astr. Soc.*, **68,** 653–673.
Yang, Y. & Ritzwoller, M., 2008. The characteristics of ambient seismic noise as a source for surface wave tomography, *Geochem. Geophys. Geosyst.*, **9**(2), Q02008, doi:10.1029/2007GC001814.
Yao, H., Gou(c)dard, P., Collins, J.A., McGuire, J.J. & van der Hilst, R.D., 2011. Structure of young East Pacific Rise lithosphere from ambient noise correlation analysis of fundamental- and higher-mode Scholte-Rayleigh waves, *C. R. Geosci.*, **343,** 571–583.

APPENDIX A: NORMAL MODE SUMMATION THEORY USING A SINGLE FORCE

In the following, we derive the elastic displacement field through normal mode summation for a spherical, symmetric, non-rotating, perfectly elastic and isotropic (SNREI) earth model. We express the elastic displacement field by normal modes summation. Because of the spherical symmetry, the eigenmodes are described by only three quantum numbers, n, l and q. n is the radial order, l is the angular order and q represents the type of mode, which can be spheroidal or toroidal. The eigenfunctions and the associated eigenfrequencies are indicated as ω_k and u_k, where k encapsulates all the quantum numbers. Following Gilbert (1970) and Aki & Richard (2002) the displacement calculated at a certain time t and at a fixed point $x = (r\sin\theta\cos\phi, r\sin\theta\sin\phi, r\cos\theta)$ can be expressed as,

$$\mathbf{s}(\mathbf{r}, t) = \sum_k \left(\int_{V_E} \mathbf{u}_k^* \cdot \mathbf{f}(\mathbf{r})\, \mathrm{d}V \right) \mathbf{u}_k\, g(t) \tag{A1}$$

where $g(t)$ is the inverse Laplace–Fourier transform of,

$$g(t) = \int \frac{f(s)}{s^2 - \omega^2} \mathrm{d}s \tag{A2}$$

which becomes $g(t) = \frac{\sin(\omega_k t)}{\omega_k} H(t - t_0)$ if we consider a point force in time $f(t) = \delta(t - t_0)$.

Moreover, if we consider a point force also in space at source coordinates $r_{0s} = (r_s, \theta_s, \phi_s)$, then the force can be written as,

$$\mathbf{f}(\mathbf{r}) = \mathbf{F}\delta(r - r_{0s}) \tag{A3}$$

Knowing the displacement (A1) and the source (A3), a general expression of a synthetic seismogram can be written introducing a so-called 'instrumental vector' v, which is a unitary displacement vector in the direction of motion (Woodhouse & Girnius 1982),

$$\mathbf{v} \cdot \mathbf{s}(\mathbf{r_r}, t) = \sum_k \left(\int_{V_E} \mathbf{u}_k^* \cdot \mathbf{f}(\mathbf{r})\, \mathrm{d}V \right) \mathbf{v} \cdot \mathbf{u}_k \frac{\sin(\omega_k t)}{\omega_k} H(t) \tag{A4}$$

$$= \sum_k R_k(\mathbf{r_r}, \theta_r, \phi_r) S_k(\mathbf{r_s}, \theta_s, \phi_s) \frac{\exp(i\omega_k t)}{\omega_k^2}, \tag{A5}$$

where $r_{0r} = (r_r, \theta_r, \phi_r)$ is the receiver position, $R_k(\mathbf{r_r}, \theta_r, \phi_r)$ is the receiver term and $S_k(\mathbf{r_s}, \theta_s, \phi_s)$ the source term.

Table A1. Source and receiver coefficients using a point force source. ${}_n\mathrm{U}_l$, ${}_n\mathrm{V}_l$ and ${}_n\mathrm{W}_l$ are the scalar eigenfunctions for a mode defined by the quantum numbers n and l evaluated at the Earth's surface for the receiver term and at the source radius for the source term. F_r, F_θ and F_ϕ are the components of the force vector and v_r, v_θ and v_ϕ are the components of the instrumental vector.

N	$\mathrm{S}_{kN}(r_s)$	$\mathrm{R}_{kN}(r_r)$
Spheroidal modes		
-1	$\gamma_l \omega_0^l (F_\Theta + iF_\Phi)_n \mathrm{V}_l$	$\gamma_l \omega_0^l (v_\Theta - iv_\Phi)_n \mathrm{V}_l$
0	$\gamma_l F_{rn} \mathrm{U}_l$	$\gamma_l v_{rn} \mathrm{U}_l$
$+1$	$\gamma_l \omega_0^l (-F_\Theta + iF_\Phi)_n \mathrm{V}_l$	$\gamma_l \omega_0^l (-v_\Theta - iv_\Phi)_n \mathrm{V}_l$
Toroidal modes		
-1	$\gamma_l \omega_0^l (-F_\Phi + iF_\Theta)_n \mathrm{W}_l$	$\gamma_l \omega_0^l (-v_\Phi - iv_\Theta)_n \mathrm{W}_l$
0	0	0
$+1$	$\gamma_l \omega_0^l (F_\Phi + iF_\Theta)_n \mathrm{W}_l$	$\gamma_l \omega_0^l (v_\Phi - iv_\Theta)_n \mathrm{W}_l$

Comparing equations (A4) and (A5) we are able to define the source and the receiver term in case of a single force,

$$S_k(r_s, \theta_s, \phi_s) = \mathbf{F} \cdot \mathbf{u}_k^*(\mathbf{r_0}) \tag{A6}$$

$$R_k(r_s, \theta_s, \phi_s) = \mathbf{v} \cdot \mathbf{u}_k(\mathbf{r_r}). \tag{A7}$$

For the analytical derivation, it is useful to expand a certain linear combination of spheroidal components of a tensor in terms of generalized spherical harmonics instead to expand the spheroidal components of a tensor directly in spherical harmonics (Phinney & Burridge 1973).

Then, a general vector can be transformed in canonical coordinates as $F^\alpha = C^\dagger_{\alpha i} u_i$, where α denote the canonical components (+, 0, −) and i the spherical components (r, θ, ϕ). $C\dagger$ is the hermitian conjugate of the matrix C,

$$C = \begin{pmatrix} 1/\sqrt{2} & 0 & -1/\sqrt{2} \\ -i/\sqrt{2} & 0 & -i/\sqrt{2} \\ 0 & 1 & 0 \end{pmatrix}.$$

The force system, the source and receiver terms can be written in canonical coordinates as well,

$$F^- = \frac{1}{\sqrt{2}}(F_\theta + iF_\phi)$$

$$F^0 = F_r \tag{A8}$$

$$F^+ = \frac{1}{\sqrt{2}}(-F_\theta + iF_\phi)$$

$$S_k(r_{0s}) = F^+ u^+ + F^0 u^0 + F^- u^- \tag{A9}$$

$$R_k(r_{0r}) = -u^+ v^- + u^0 v^0 - u^- v^+. \tag{A10}$$

Following the approach of Phinney & Burridge (1973), that is using the canonical coordinates, we are now able to rewrite the com-

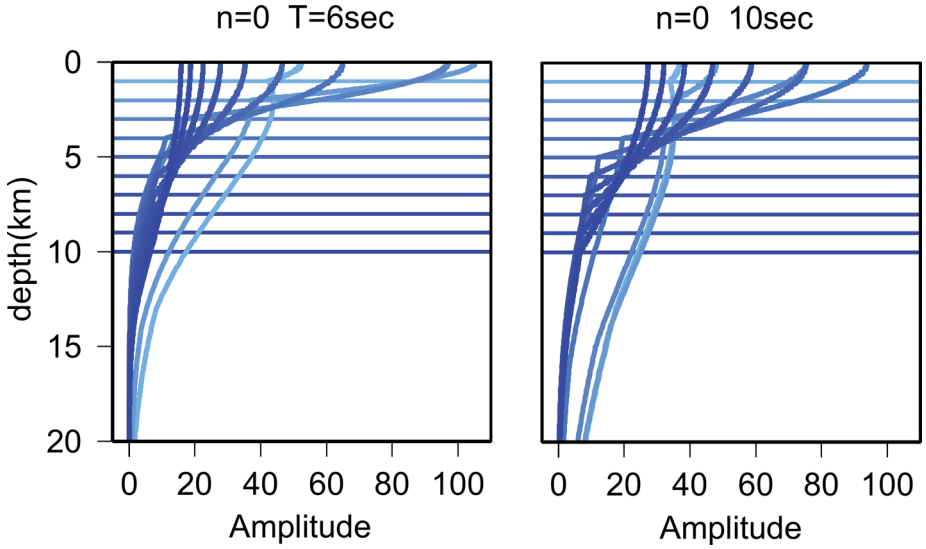

Figure A1. Eigenfunctions of Rayleigh waves fundamental mode for a period of 6 and 10 s computed by using PREM model in which we set 10 different ocean depths. The horizontal lines represent the ocean seafloor of each model and their colours are linked with the colour of the respective eigenfunctions. We observe that the energy is not confined within the ocean layer.

ponents of the displacement **u** introducing the generalized spherical harmonics $Y_k^N(\theta, \phi)$, with $N = (+, 0, -)$,

$$u^- = \gamma_l \omega_0^l (V_k - i W_k) Y_k^-$$

$$u^0 = \gamma_l U_k Y_k^0$$

$$u^+ = \gamma_l \omega_0^l (V_k + i W_k) Y_k^+,$$

where $\omega_0^l = \sqrt{\frac{l(l+1)}{2}}$. The normalization coefficient $\gamma_l = \sqrt{\frac{2l+1}{4\pi}}$ has been found out by applying the orthogonality relation of spherical harmonics (Phinney & Burridge 1973).

In Table A1, we summarize the source S_{kN} and the receiver term R_{kN}, respectively defined by eqs (A9) and (A10), in canonical coordinates for a case of a general point force.

If we consider a purely vertical force, because of the definition of the force itself (A8) in canonical coordinates, the unique non-null component of the source term is

$${}_n\mathrm{S}_l^0(r_s, \Theta_s, \Phi_s) = \gamma_l \; F_r(\mathbf{r}_s) \, \mathrm{U}_k(\mathbf{r_s}) \; Y_k^0(\Theta_s, \Phi_s). \tag{A11}$$

The analytical expression of the vertical component of the synthetic seismogram in case of a vertical force can be easily written from eq. (A5),

$$\begin{aligned} \mathbf{v} \cdot \mathbf{s} &= \mathbf{u}(\mathbf{r}, \theta, \phi) \\ &= \gamma_l^2 \; F_r(\mathbf{r}_s) \, v_r \, \mathrm{U}_k(\mathbf{r_s}) \, \mathrm{U}_k(\mathbf{r_r}) \; Y_k^0(\Theta_s, \Phi_s) Y_k^0(\Theta_r, \Phi_r) \exp(i \omega_k t). \end{aligned} \tag{A12}$$

Due to the vertical point force and the SNREI model only Rayleigh waves, *P* and *SV*, are excited and recorded at any station.

In Fig. A1 we show the eigenfunctions *U* of the Rayleigh waves fundamental mode as a function of depth for two periods, 6 and 10 s. We compute them by using PREM model in which we change the thickness of the ocean layer. Horizontal lines represent each ocean seafloor. We use the same colour for the eigenfunction and the model in which they are computed, identified by the colour of the ocean seafloor. We observe that the eigenfunctions of the fundamental mode of Rayleigh waves show a cusps at the seafloor. They are strongly sensitive to the ocean layer (e.g. Yao *et al.* 2011), but the amplitude is still significant below the water layer, meaning that the energy is not confined within the ocean.